Inorganic Chemistry Communications 188 (2026) 116525

Contents lists available at ScienceDirect

Inorganic Chemistry Communications

journal homepage: www.elsevier.com/locate/inoche

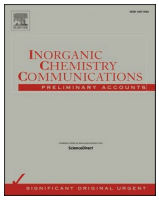

Research Article

Green-synthesised NH_2-MIL-101(Cr) MOF–reinforced starch bioplastic films for sustainable food packaging

Shima Jafarzadeh [a,*], Yasaman Esmaeili [b], Moon Paul [c], Seyedeh Zahra Haeri [d], Colin J. Barrow [a,e], Mina Dokouhaki [f], Masoumeh Zargar [d,*], Minoo Naebe [c,*]

[a] Centre for Sustainable Bioproducts, Deakin University, Geelong, Victoria 3216, Australia
[b] School of Engineering, Deakin University, Geelong, Victoria 3216, Australia
[c] Institute for Frontier Materials (IFM), Deakin University, Waurn Ponds, VIC 3216, Australia
[d] School of Engineering, Edith Cowan University, 270 Joondalup Drive, Joondalup, WA 6027, Australia
[e] Distinguished Research Fellow, College of Health Sciences, Abu Dhabi University, Abu Dhabi 59911, United Arab Emirates
[f] Food Research and Innovation Center, School of Science, RMIT University, Bundoora, Victoria, Australia

ARTICLE INFO

Keywords:
Green synthesis
Metal organic frameworks (MOF)
Sago starch
Bioplastic films
Sustainable packaging

ABSTRACT

This study introduces a green, aqueous synthesis approach for NH_2-MIL-101(Cr), avoiding toxic organic solvents while preserving its high crystallinity, porosity (>1000 m^2/g), and amino functionality. To develop sustainable packaging materials the synthesized MOF was incorporated into sago starch-based bioplastic films across control 0%, 1%, 3%, and 5% treatments. Nanoparticle characterizations via SEM, TEM, FTIR, XRD, and nitrogen adsorption-desorption isotherms confirmed a porous, crystalline structure (100–300 nm) with a surface area exceeding 1000 m^2/g. Film characterizations using SEM, FTIR, color analysis, tensile testing, TGA, and UV-Vis spectroscopy revealed that the 3% treatment offered the best balance, with tensile strength increasing from 2.15 MPa (control) to 4.61 MPa, thermal stability improving (decomposition onset from 230 °C to 270 °C), and UV shielding enhancing (>83% transmittance at 600 nm). The 5% treatment achieved the highest tensile strength (4.84 MPa) but showed reduced elongation (45.59% vs. 125.16% in control) due to agglomeration, while 1% provided moderate improvements. These results underscore the 3% treatment as the most suitable for eco-friendly packaging, with future work recommended to optimize MOF dispersion, extend UV analysis, and evaluate biodegradability for industrial scalability.

1. Introduction

The global packaging industry relies heavily on synthetic plastics, generating over 300 million tons of waste annually. These durable materials degrade slowly and often leach toxic additives, causing persistent environmental and health problems. Bioplastics, polymers made from renewable resources, offer a sustainable alternative with reduced fossil fuel demand, smaller carbon footprint, and faster biodegradation [1]. However, conventional biopolymer films typically suffer from lower mechanical strength and barrier performance compared to petroleum-based plastics. To overcome these limitations, advanced biocomposite systems are being developed that incorporate functional nanoscale fillers to enhance performance [2].

Among potential nanofillers, metal–organic frameworks (MOFs) have emerged as particularly promising for food packaging applications [3,4]. MOFs are crystalline, porous networks with extremely high surface area and tunable chemistry [5]. When dispersed in a polymer matrix, MOFs can simultaneously improve mechanical strength and barrier properties and introduce active functions (e.g. antimicrobial action or controlled release of preservatives) to extend shelf life. In this context, the amino-functionalized chromium MOF NH_2-MIL-101(Cr) is especially attractive: it exhibits exceptional thermal and chemical stability, a specific surface area well above 1000 m^2/g, and reactive —NH_2 groups that can enhance compatibility with biopolymers [6]. Recently, metal–organic frameworks (MOFs), a class of porous hybrid supramolecular materials, have been developed as an active agent to extend food shelf life through their unique combination of high porosity, tunable functionality, and controlled release capabilities [6]. MOFs are functional materials with special physical and chemical properties, such as a high specific surface area, high porosity and adjustable structure, which can

* Corresponding authors.
E-mail addresses: s.jafarzadeh@deakin.edu.au (S. Jafarzadeh), m.zargar@ecu.edu.au (M. Zargar), minoo.naebe@deakin.edu.au (M. Naebe).

https://doi.org/10.1016/j.inoche.2026.116525
Received 1 December 2025; Received in revised form 28 January 2026; Accepted 14 March 2026
Available online 17 March 2026

be designed and adjusted according to the characteristics of different food packaging materials, making them ideal candidates for advanced packaging applications. For example, Ananthi et al., (2023) [7] and Riahi et al., (2023) [8]developed cellulose acetate and gelatin films with Fe-MIL-88A and ZIF-8, respectively, improving tensile strength and antimicrobial activity, while Khan et al., (2021) [9] and Huang et al., (2024) [10] enhanced PVA/starch films with ZIF-67 and Cu-ICA for thermal stability and intelligent freshness monitoring. Jafarzadeh, Golgoli, et al., (2024) [11] incorporated Ce-MOF into cassava starch films, increasing crystallinity, hydrophobicity, and thermal stability for active packaging. Similarly, An et al., 2024 [12], Jiang et al., 2022 [13] and Khan et al., (2023) [14] utilized *Cordyceps militaris*, zein, and gelatin/carrageenan matrices with MOFs for biodegradability and active packaging and Zhao et al., (2023) [15] and Zhang et al., (2023) [16] and Hong et al., (2025) [17] incorporated MOFs into synthetic or semi-renewable polymers for fruit and shrimp preservation.

Despite these advantages, conventional synthesis of NH_2-MIL-101 (Cr) relies on toxic organic solvents (such as dimethylformamide or diethylformamide) that undermine sustainability. There is a critical need for green, water-based synthetic routes that preserve the MOF's structure and functionality [18]. Some recent studies have demonstrated solvent-free or aqueous syntheses for other MOFs [19,20], but fully aqueous preparation of NH_2-MIL-101(Cr) with high crystallinity and amine functionality has not been reported. Similarly, the use of abundant natural polymers like sago starch, a high-amylose starch with minimal food-crop conflict, as a matrix for water-synthesized MOFs has not been systematically explored [18]. This work addresses these gaps by developing an optimized, solvent-free (aqueous) synthesis of NH_2-MIL-101(Cr) and incorporating the resulting MOF into sago starch-based bioplastic films. We investigate how varying MOF loadings (0–5 wt%) affect the films' mechanical strength, thermal stability, and UV-shielding performance. By eliminating organic solvents in MOF production and using a biodegradable starch matrix, our approach aims to create scalable, eco-friendly MOF–starch composites suitable for sustainable food packaging.

2. Methods and materials

2.1. Materials

Chromium (III) nitrate nonahydrate ($Cr(NO_3)_3{\cdot}9H_2O$, ≥98%) and 2-aminoterephthalic acid ($H_2BDC\text{-}NH_2$, ≥99%) were used as precursors for NH_2-MIL-101(Cr) synthesis, sourced from Merck. Sodium hydroxide (NaOH, ≥98%) and hydrochloric acid (HCl, 37%) for pH adjustment were obtained from Merck. Sago starch (food-grade, amylose content ~27%) was extracted from the local market. Glycerol (≥99.5%, food-grade) served as a plasticizer, purchased from Merck. Deionized water was used as the solvent for MOF synthesis and film preparation. All chemicals were used as received without further purification.

2.2. Green synthesis of NH_2-MIL-101(Cr)

NH_2-MIL-101(Cr) was synthesized via a green aqueous method adapted from Chen et al. (2019) to eliminate the use of organic solvents. A solution of 2-aminoterephthalic acid (0.45 g, 2.5 mmol) was prepared in 50 mL deionized water, and the pH was adjusted to 6.5 using 0.1 M NaOH with stirring at 500 rpm for 30 minutes to ensure complete dissolution. Separately, chromium(III) nitrate nonahydrate (1.0 g, 2.5 mmol) was dissolved in 50 mL deionized water. The chromium solution was slowly added to the ligand solution under continuous stirring at 500 rpm, and the pH of the mixture was maintained at 6.5–7.0 using 0.1 M NaOH or 0.1 M HCl as needed. The mixture was then transferred to a Teflon-lined stainless-steel autoclave and heated at 150 °C for 12 h. Alternatively, for room-temperature synthesis, the reaction was allowed to proceed at 25 ± 2 °C for 24 h under continuous stirring. After the reaction, the resulting green precipitate was collected by centrifugation at 8000 rpm for 10 minutes, washed three times with deionized water to remove unreacted precursors, and dried at 60 °C for 12 h. The synthesized NH_2-MIL-101(Cr) was stored in a desiccator until further use and characterized for crystallinity, functionality, and morphology [21].

Table 1
Experimental treatments for sago starch-based bioplastic films with varying NH_2-MIL-101(Cr) concentrations.

Treatment	Description
Control	Sago starch film with 0% NH_2-MIL-101(Cr), containing 4 g sago starch and 40 wt% glycerol as plasticizer.
MOF 1%	Sago starch film with 1 wt% NH_2-MIL-101(Cr) (based on dry starch weight), with 4 g sago starch and 40 wt% glycerol.
MOF 3%	Sago starch film with 3 wt% NH_2-MIL-101(Cr) (based on dry starch weight), with 4 g sago starch and 40 wt% glycerol.
MOF 5%	Sago starch film with 5 wt% NH_2-MIL-101(Cr) (based on dry starch weight), with 4 g sago starch and 40 wt% glycerol.

2.3. Preparation of Sago starch-based bioplastic films

Sago starch-based bioplastic films were prepared via solution casting with four treatments: Control (0% MOF), MOF 1%, MOF 3%, and MOF 5%, as detailed in Table 1. Sago starch (5 g) was dispersed in deionized water (100 mL) and heated at 85 °C while stirring at 300 rpm until complete gelatinization (approximately 30 minutes). Glycerol (30 wt% based on starch) was added as a plasticizer, and the mixture was stirred for 15 minutes at 70 °C. For the MOF treatments, NH_2-MIL-101(Cr) was dispersed in deionized water (10 mL) via ultrasonication (40 kHz, 30 minutes) at concentrations corresponding to 1, 3, and 5 wt% (based on dry starch weight). The MOF dispersion was added to the gelatinized starch solution and stirred for 30 minutes at 60 °C to ensure homogeneous dispersion. For the Control treatment, no MOF was added. Each mixture was degassed to remove air bubbles, cast onto glass plates (20 × 20 cm), and dried at 40 °C for 24 h in a ventilated oven. The films were peeled off and conditioned at 25 °C and 50% relative humidity for 48 h before testing [22] Fig. 1 shows the schematic process developed for green synthesis of NH_2-MIL-101 and Fig. 2a–c illustrate the visual bioplastic films (c), the MOF nanomaterial powder incorporated into the formulation (d), and the starch film-forming solutions with varying MOF concentrations that were prepared prior to casting the films (e).

2.4. Multifunctional characterization of NH_2-MIL-101(Cr) nanoparticles and bioplastic films

The internal structure and particle size distribution of NH_2-MIL-101 (Cr) and bioplastic films (Control, MOF 1%, MOF 3%, and MOF 5%) were examined using TEM, JEM-2100F Field Emission Electron Microscope. A small quantity of the MOF powder was dispersed in deionized water and sonicated for 30 minutes to achieve a homogeneous suspension. A drop of this suspension was then placed onto a carbon-coated copper grid and allowed to air-dry. The grid was inserted into the microscope, which was operated at an accelerating voltage of 200 kV [23]. The specific surface area, pore volume, and pore size distribution of NH_2-MIL-101(Cr) were measured using Gas Absorption Analysis, BET/BJH (Quantachrome, Autosorb iQ)-001 analyzer at 77 K. Prior to analysis, approximately 100 mg of the MOF sample was degassed at 150 °C for 6 h under vacuum to remove adsorbed moisture and gases. The adsorption-desorption isotherms were recorded, and the Brunauer-Emmett-Teller (BET) method was applied to calculate the specific surface area [24]. The optical properties and UV-blocking ability of the sago starch-based bioplastic films (Control, MOF 1%, MOF 3%, and MOF 5%) were evaluated using an UV-Vis spectrophotometer (Cary 300). Film samples were cut into 4 cm × 4 cm squares and placed in the sample holder. Transmittance spectra were recorded in the wavelength range of 200–800 nm [25].

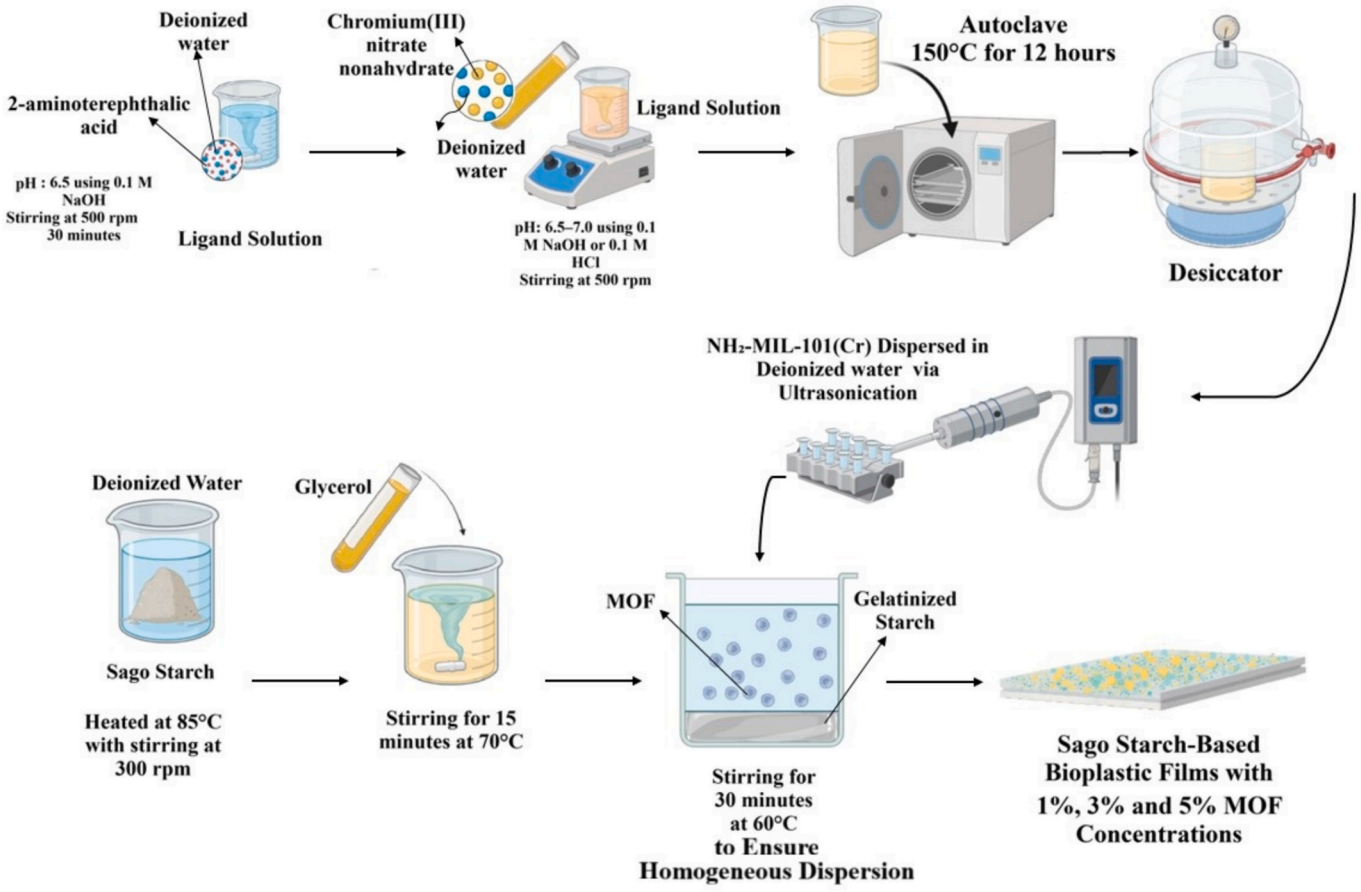

Fig. 1. The schematic process developed for green synthesis of NH_2-MIL-101(Cr), followed by preparation of sago starch-based bioplastic films containing MOF.

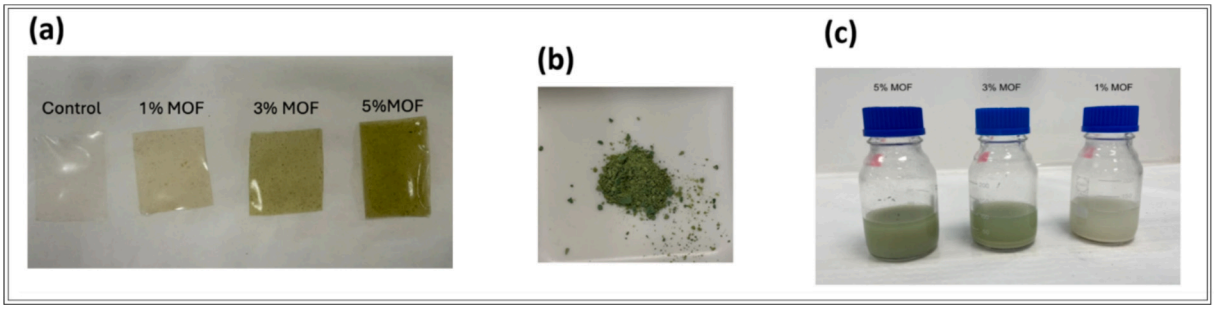

Fig. 2. (a) Prepared bioplastic films; (b) MOF nanomaterial powder; (c) Starch-based film-forming solutions containing different MOF concentrations for film preparation.

2.5. Microstructure and chemical properties NH_2-MIL-101(Cr) nanoparticles and bioplastic films

The microstructural and chemical properties of the samples were analyzed using Fourier Transform Infrared Spectroscopy (FTIR), X-ray Diffraction (XRD), and Scanning Electron Microscopy (SEM). The surface morphology and particle size of NH_2-MIL-101(Cr) nanoparticles and bioplastic films (Control, MOF 1%, MOF 3%, and MOF 5%) were analyzed using ZEISS Gemini SEM 460 field-emission SEM. Samples were prepared by dispersing a small amount of the synthesized MOF powder onto a conductive carbon tape mounted on an aluminum stub. To enhance conductivity and prevent charging during imaging, the samples were sputter-coated with a thin layer of gold under vacuum. The microscope was operated at an accelerating voltage of 15 kV, and images were captured at various magnifications to observe the particle shape, size distribution, and surface characteristics of the MOF [26].

The chemical composition and functional groups of NH_2-MIL-101 (Cr) were characterized using Bruker INVENIO FT-IR spectrometer. For the MOF, samples were prepared by mixing the powder with potassium bromide (KBr) and pressing the mixture into a thin pellet. For the bioplastic films, samples were directly placed on the attenuated total reflectance (ATR) crystal. Spectra were collected in the wavenumber range of 400–4000 cm^{-1} with a resolution of 4 cm^{-1}, averaging 32 scans to ensure high signal-to-noise ratio [16]. The crystallinity and phase purity of NH_2-MIL-101(Cr) and bioplastics were determined using Empyrean PW3373/00 Cu LFF DK435004 source. The MOF powder was finely ground and uniformly spread onto a sample holder to ensure a flat surface. The diffractometer was operated with Cu Kα radiation (λ = 1.5406 Å) at 40 kV and 40 mA, and diffraction patterns were collected over a 2θ range of 5–50° at a scan rate of 0.02°/s [27].

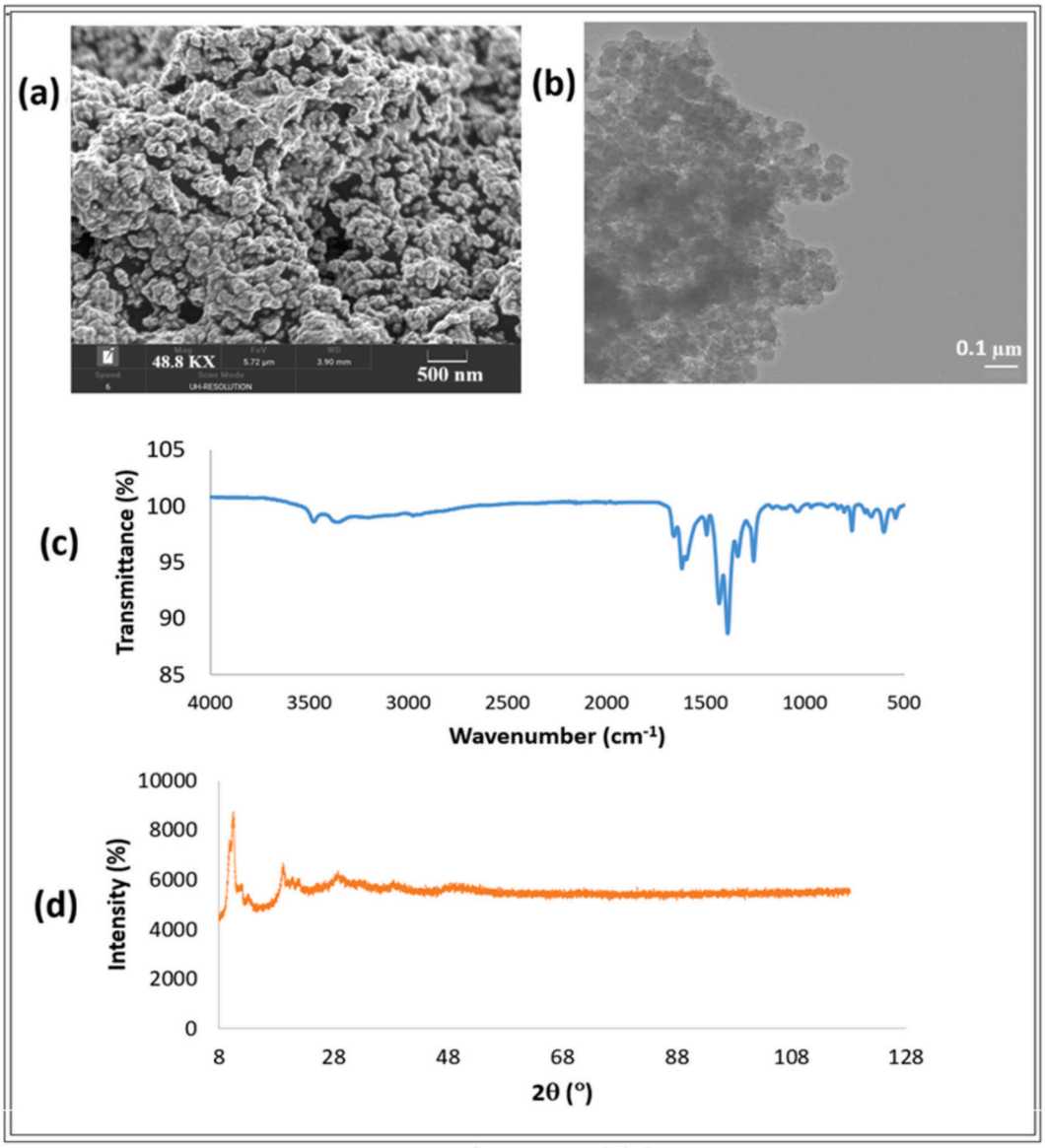

Fig. 3. Morphological structure biofilms: (a) SEM image of NH_2-MIL-101(Cr) nanoparticles synthesized via green aqueous method, captured at a magnification of 48,800×, (b) TEM image of NH_2-MIL-101(Cr) nanoparticles synthesized via green aqueous method, captured at a magnification of 100,000x. (c) FTIR spectrum of NH_2-MIL-101(Cr) nanoparticles synthesized via green aqueous method, recorded in the wavenumber range of 400–4000 cm^{-1}. (d) X-ray Diffraction (XRD) Pattern of NH_2-MIL-101(Cr) Nanoparticles.

2.6. Color measurement

The color properties of the sago starch-based bioplastic films (Control, MOF 1%, MOF 3%, and MOF 5%) were evaluated using a Spectrophotometer, Color (Datacolor, 600)-001colorimeter based on the L*ab** color system. Film samples were placed on a standard white background, and measurements were taken at five random locations on each film to ensure reproducibility [28].

2.7. Thermal and mechanical properties evaluation

2.7.1. Mechanical properties

The mechanical properties, including tensile strength, elongation at break, and Young's modulus, of the sago starch-based bioplastic films (Control, MOF 1%, MOF 3%, and MOF 5%) were measured using an Instron universal testing machine in accordance with ASTM D882-18. Film samples were cut into strips (10 cm × 2.5 cm) and tested with a crosshead speed of 50 mm/min and an initial grip distance of 50 mm [29]. To describe the combined effect of tensile strength and elongation at break, a Property Balance Index (PBI) was calculated as the product of tensile strength (σ, MPa) and elongation at break (ε_b, %) [30].

$$PBI = \sigma \times \varepsilon\_b \quad (1)$$

This index was used to compare the overall mechanical balance of the films.

2.7.2. Thermogravimetric analysis (TGA)

The thermal stability of the sago starch-based bioplastic films (Control, MOF 1%, MOF 3%, and MOF 5%) was assessed using thermogravimetric analyzer (TGA) Discovery 550 Auto from TA Instruments. Approximately 5–10 mg of each film sample was placed in a ceramic crucible and heated from 30 °C to 600 °C at a heating rate of 10 °C/min under a nitrogen atmosphere with a flow rate of 50 mL/min [31].

2.8. Statistical analysis

All characterization tests were performed in triplicate, unless otherwise specified (e.g., five replicates for tensile testing), and results were expressed as mean ± standard deviation. Data was analyzed using SPSS software (version 25). One-way analysis of variance (ANOVA) was conducted to determine significant differences among the treatments (Control, MOF 1%, MOF 3%, MOF 5%) for each measured parameter (e.g., tensile strength, contact angle, UV transmittance). When significant differences were detected ($p < 0.05$), Duncan's multiple range test was applied for post-hoc comparisons to identify specific differences between treatment means. The significance level was set at $\alpha = 0.05$ for all analyses.

3. Results and discussion

3.1. Surface morphology of NH_2-MIL-101(Cr) nanoparticles using SEM

The surface morphology of the synthesized NH_2-MIL-101(Cr) nanoparticles was investigated using SEM, with the image captured at a magnification of 48,800x and a scale bar of 500 nm (Fig. 3a). The image revealed a porous, cluster-like structure with a rough texture, indicative of nanoparticle aggregation. The particle size was estimated to range from approximately 100 to 300 nm, consistent with the scale bar, suggesting a nanoscale distribution suitable for incorporation into bioplastic matrices. The observed porosity and roughness are characteristic of the MIL-101(Cr) framework, supporting its high specific surface area, which is critical for enhancing interactions with the sago starch matrix in packaging applications.

Kowsar et al. (2025) reported a porous structure for NH_2-MIL-101 (Cr) in epoxy adhesives, consistent with the morphology in this study, although the particle size range (100–300 nm) may reflect a broader distribution due to differences in synthesis conditions or post-processing techniques. The porosity aligns with the reported surface area exceeding 1000 m^2/g, validating the efficacy of the green synthesis approach employed [32]. Yunus et al. (2024) reported SEM analysis of MIL-101-Fe MOF powders, revealing irregular particle shapes and sizes, like the scattered and clustered morphology observed in our MOF 1% and 3% samples, with increased density at higher loadings akin to our MOF 5% [33]. Wu et al. (2019) characterized Zn@MOF powders using SEM, noting porous, crystalline structures with particle aggregation, consistent with the cluster formation in our samples, particularly at 3% and 5%, which may support antimicrobial applications [34]. Yang et al. (2020) described SEM images of magnetic MOF (MMOF) powders showing varied particle sizes and distributions, aligning with the concentration-dependent trends in our study, suggesting potential for food contaminant extraction [16].

3.2. Internal structure NH_2-MIL-101(Cr) nanoparticles using TEM

The internal structure and particle size distribution of the NH_2-MIL-101(Cr) nanoparticles were examined using TEM, with the image captured at a magnification of 100,000x and a scale bar of 200 nm (Fig. 3b). The image revealed a highly porous internal structure with well-defined lattice fringes, indicating a crystalline nature. The nanoparticles exhibited an average size of approximately 150–250 nm, with some aggregation observed, consistent with the SEM findings. The presence of lattice fringes suggests a high degree of crystallinity, which is essential for the structural stability of the MOF in applications such as bioplastic reinforcement. The TEM image confirms the crystalline and porous internal structure of NH_2-MIL-101(Cr) nanoparticles, validating the green synthesis method's ability to maintain the MOF's structural integrity. The lattice fringes observed indicate a high degree of order, which is crucial for mechanical reinforcement in bioplastic films.

Zhu et al. (2017) utilized TEM to reveal the crystalline structure of ZIF-8, noting lattice fringes and porosity, which are comparable to the observations here, though the MOF type differs [35]. The slight aggregation observed in this study may contrast with the more uniform structures reported by Turner et al. (2008) for MOF-5, where TEM showed well-dispersed metal nanoparticles within the framework, possibly due to differences in synthesis and sample preparation (e.g., drying at 60 °C vs. gas-phase loading) [36]. Patterson et al. (2015) demonstrated in situ TEM growth of MOFs, observing crystalline growth with porosity, which supports the lattice fringe visibility in this study, though their focus was on dynamic growth rather than static structure [4]. Zhang et al. (2022) emphasized the beam sensitivity of MOFs, noting that low-dose TEM can reveal crystallinity, aligning with the methodology used here to preserve the NH_2-MIL-101(Cr) structure [37]. Denny et al. (2018) highlighted surface deposition in MOFs, but the internal crystallinity observed here suggests minimal surface coating, focusing on the bulk structure [38]. The porosity and crystallinity are consistent with the high surface area reported by Kowsar et al. (2025), reinforcing the material's potential for composite applications [39].

3.3. Chemical composition of NH_2-MIL-101(Cr) nanoparticles using FTIR

The chemical composition and functional groups of the NH_2-MIL-101 (Cr) nanoparticles were analyzed using FTIR spectroscopy, with spectra recorded in the wavenumber range of 400–4000 cm^{-1}. The FTIR spectrum exhibited characteristic absorption bands confirming the presence of the MOF framework. A broad band at 3400–3500 cm^{-1} was attributed to the N-H stretching of the amino (-NH_2) groups from the 2-aminoterephthalic acid ligand, while strong bands at 1650 cm^{-1} and 1380 cm^{-1} corresponded to the asymmetric and symmetric stretching of the carboxylate (COO^-) groups, respectively. A weaker band at 1250 cm^{-1} indicated C-N stretching, and bands in the 500–800 cm^{-1} region were assigned to Cr-O stretching vibrations, confirming the metal-ligand coordination in the MIL-101(Cr) structure (Fig. 3c).

Compared to previous studies, the observed bands are consistent with Xiao et al. (2025), who reported similar FTIR features for NH_2-MIL-101(Fe, Co), with N-H stretching at 3400–3500 cm^{-1} and carboxylate stretching at 1650 cm^{-1} and 1380 cm^{-1}, indicating the retention of the aminoterephthalic acid framework despite bimetallic incorporation [40]. Peens (2017) also identified these bands for NH_2-MIL-101(Al), with N—H stretching at 3400–3500 cm^{-1} and carboxylate stretching at 1650 cm^{-1} and 1380 cm^{-1}, further validated by amide bond formation post-encapsulation, though the Al—O region was not detailed. Noorani et al. (2025) reported comparable N—H and carboxylate bands for NH_2-MIL-53(Al) in MMMs, with slight shifts due to ionic liquid interactions, but lacked emphasis on metal-oxygen bands [41]. The Cr—O stretching at 500–800 cm^{-1} aligns with the metal-ligand coordination reported by Chen et al. (2019) for NH_2-MIL-101(Cr), distinguishing it from the Fe-Co, Al, and Al-based systems [41].

3.4. Crystallographic analysis of NH_2-MIL-101(Cr) nanoparticles using XRD

The crystallographic structure of the NH_2-MIL-101(Cr) nanoparticles was characterized using X-ray diffraction (XRD) analysis, with patterns recorded over a 2θ range of 5° to 50° using Cu Kα radiation ($\lambda = 1.5406$ Å) (Fig. 3d). The XRD pattern exhibited distinct diffraction peaks at 2θ values of approximately 5.2°, 8.4°, 9.0°, 10.3°, and 16.5°, corresponding to the (311), (400), (331), (422), and (822) planes, respectively, of the cubic MIL-101(Cr) framework. These peaks are indicative of the highly crystalline nature of the synthesized nanoparticles, consistent with the lattice fringes observed in TEM. The sharp and well-resolved peaks suggest a high degree of long-range order, with no significant amorphous phases detected. The peak positions and relative intensities align with the standard pattern for MIL-101(Cr), confirming the retention of the framework structure despite the green aqueous synthesis method. A slight broadening of the peaks, particularly at higher angles, may indicate a nanoscale particle size (150–250 nm), consistent with SEM and

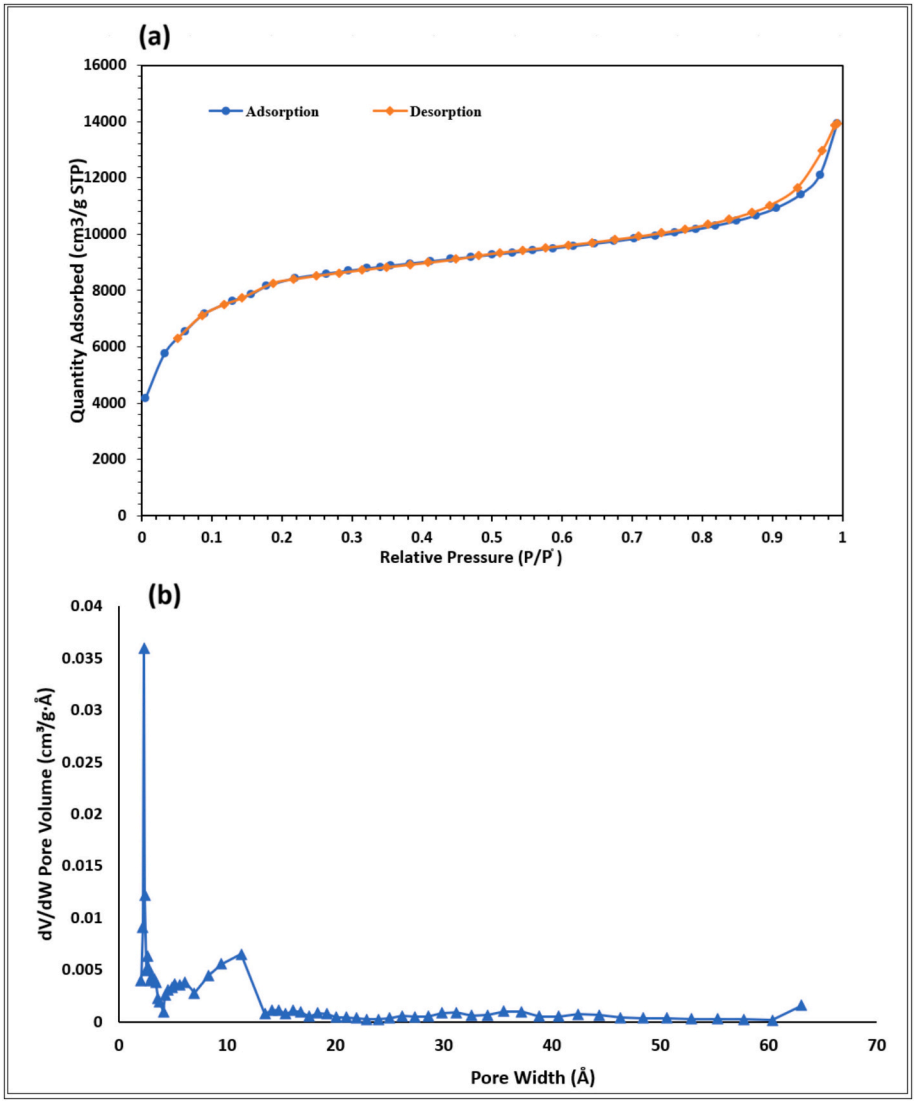

Fig. 4. (a) Nitrogen (N_2) adsorption–desorption isotherm of the green-synthesized NH_2-MIL-101(Cr). (b) Pore size distribution of NH_2-MIL-101(Cr), plotted as differential pore volume (dV/dW) versus pore width (nm).

TEM observations, and potential minor lattice strain due to the incorporation of amino groups.

The XRD pattern confirms the highly crystalline cubic structure of NH_2-MIL-101(Cr) nanoparticles synthesized via the green aqueous method, with diffraction peaks at 5.2°, 8.4°, 9.0°, 10.3°, and 16.5° matching the (311), (400), (331), (422), and (822) planes of the MIL-101 framework. This crystallinity supports the lattice fringe observations from TEM and validates the structural integrity maintained under the solvent-free conditions at 150 °C for 12 h. The consistency with Chen et al. (2019) suggests that the green synthesis effectively replicates the hydrothermal method's crystalline outcome, despite the absence of organic solvents. The slight peak broadening, particularly at higher angles, is indicative of nanoscale dimensions (150–250 nm), aligning with SEM and TEM data, and may reflect minor lattice strain from the amino functionalization, which could enhance the material's interaction with the sago starch matrix [42]. Compared to results from Xiao et al. (2025) [40], the retention of the cubic structure is similar, though their bimetallic NH_2-MIL-101(Fe, Co) showed minor peak shifts due to lattice distortion from Co incorporation, a feature not observed here with the monometallic Cr framework. Peens (2017) reported a comparable cubic structure for NH_2-MIL-101(Al), with slightly higher 2θ values, likely due to differences in metal-oxygen bond lengths (Al-O vs. Cr-O), and their high BET surface area supports the porosity seen in this study. Noorani et al. (2025) [41] highlighted a different orthorhombic structure for NH_2-MIL-53(Al), with broader peaks reflecting a less ordered framework, contrasting with the sharp peaks of MIL-101(Cr) and underscoring the topological distinction between MIL-101 and MIL-53. The absence of extraneous peaks suggests high phase purity, reinforcing the efficacy of the green synthesis. These crystallographic features are expected to contribute to the mechanical stability and photocatalytic potential of the nanoparticles in bioplastic composites, with further analysis of film properties to follow.

3.5. Isotherm analysis

Isotherm analysis is used for characterizing the porous structure of nanomaterials, such as metal-organic frameworks (MOFs) like NH_2-MIL-101(Cr). This analysis provides insights into surface area, pore size distribution, and adsorption-desorption behavior, which are essential for applications in gas storage, catalysis, and separation processes. The nitrogen adsorption-desorption isotherm enables the identification of mesoporous characteristics and the presence of hysteresis loops, which reveal pore geometry and connectivity. Understanding these properties is essential to optimize material performance, making this analysis

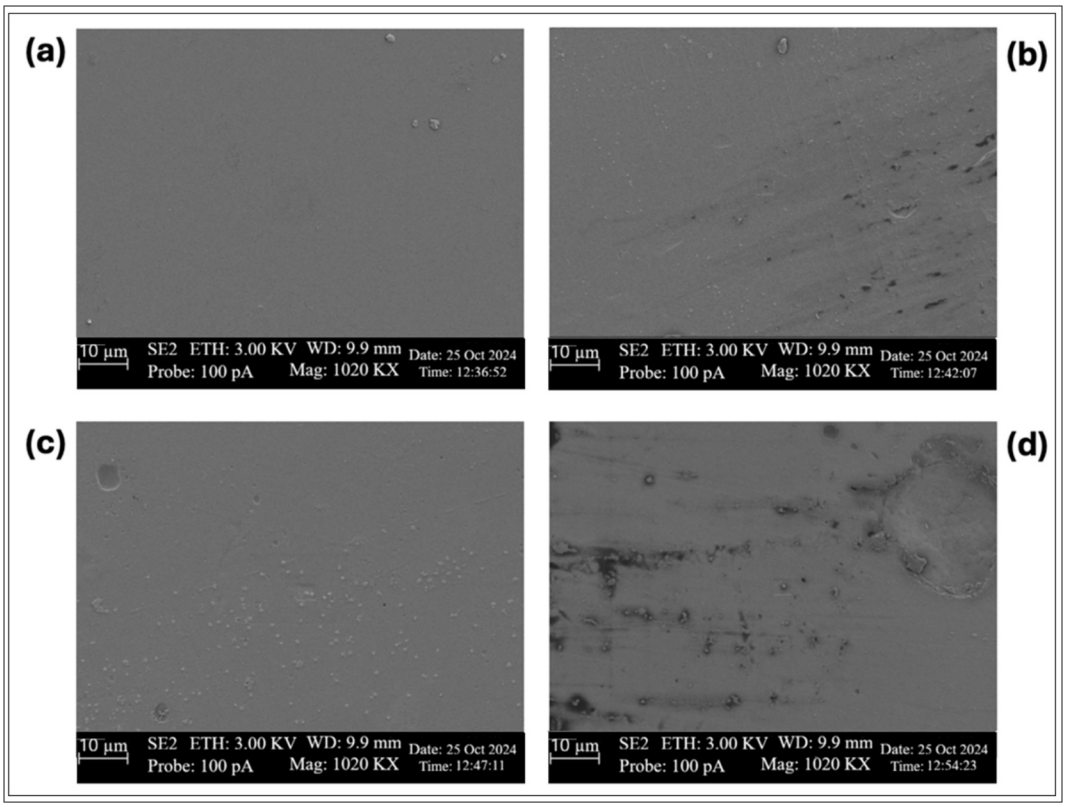

Fig. 5. SEM Images of control and NH_2-MIL-101(Cr) Bioplastic Morphology at Different Concentrations: (a) control, (b) MOF 1%, (c) MOF 3%, (d) MOF 5% (Mag~ 10k), showing concentration-dependent dispersion and agglomeration of MOF particles.

important in the development of advanced materials. The nitrogen adsorption-desorption isotherm of NH_2-MIL-101(Cr) nanoparticles, obtained using the Micromeritics TriStar II 3020 at 77.300 K, is presented in Fig. 4a. This isotherm exhibits a Type IV profile with a distinct hysteresis loop, characteristic of mesoporous materials. The data covers a relative pressure (P/P_o) range from 0.0048 to 0.99 for adsorption and from 0.99 to 0.0515 for desorption, with the adsorbed quantity ranging from 229.45 to 770.08 cm^3/g STP for adsorption and 766.8139845 to 348.2790108 cm^3/g STP for desorption.

The adsorption branch begins at a low relative pressure (P/P_o = 0.0048) with a quantity adsorbed of 229.45 cm^3/g STP, indicating initial multilayer formation and a minor microporous contribution. As P/P_o increases, the adsorbed quantity rises steadily, reaching 420.75 cm^3/g STP at P/P_o = 0.13, suggesting monolayer completion. A significant upturn occurs beyond P/P_o = 0.4, where the quantity adsorbed reaches 494.60 cm^3/g STP, marking the onset of capillary condensation within the mesopores. The curve continues to rise sharply, peaking at 770.08 cm^3/g STP at P/P_o = 0.99, reflecting the filling of mesopores and multilayer adsorption at near-saturation conditions.

The desorption branch starts at P/P_o = 0.99 with a quantity adsorbed of 766.82 cm^3/g STP, slightly below the adsorption maximum due to proximity to saturation. As P/P_o decreases, the desorption curve tracks the adsorption path until $P/P_o \approx 0.94$ (643.50 cm^3/g STP), after which it diverges, initiating the hysteresis loop. The desorption quantity decreases gradually, dropping to 541.69 cm^3/g STP at P/P_o = 0.675, and further to 348.28 cm^3/g STP at P/P_o = 0.051, corresponding to the emptying of mesopores.

The hysteresis loop, clearly depicted in Fig. 4a, is observed between $P/P_o \approx 0.4$ and 0.9, a hallmark of mesoporous materials. At P/P_o = 0.4, the adsorbed quantity for adsorption is 494.60 cm^3/g STP, while for desorption it is 541.69 cm^3/g STP, indicating a difference of approximately 47 units. This divergence increases slightly at P/P_o = 0.9, where adsorption reaches 603.53 cm^3/g STP and desorption is 548.11 cm^3/g STP, a difference of about 55 units. The loop narrows and closes near P/P_o = 0.9, where the curves converge due to near-saturation multilayer adsorption. This H2-type hysteresis suggests ink-bottle-shaped pores, were narrow necks delay desorption.

The Type IV isotherm with an H2 hysteresis loop, as shown in Fig. 4a, confirms that NH_2-MIL-101(Cr) possesses a well-defined mesoporous architecture. The initial gradual increase at low P/P_o indicates a minor microporous contribution, while the steep rise between 0.4 and 0.9 P/P_o reflects capillary condensation within mesopores. The hysteresis loop's shape suggests complex pore geometries with narrow necks and wider bodies, impeding desorption, which is consistent with the mesoporous nature of the material. In addition, the pore size distribution obtained from the desorption branch (Fig. 4b) shows a main pore diameter centered at approximately 3–4 nm, corresponding to the characteristic cages of the MIL-101(Cr) framework, with a smaller contribution from micropores below 2 nm. This pore structure offers a large surface area that enhances interaction between the MOF and the starch matrix.

This behavior aligns with that observed by Zhang et al. (2019), who studied amine-functionalized MOF-199 for H_2S adsorption, noting a Type IV isotherm with a hysteresis loop like NH_2-MIL-101(Cr) in N_2 isotherms. The enhanced H_2S capacity in TEA/MOF-199 (2.74 mmol/g) due to hydroxyl interactions mirrors the high N_2 capacity of NH_2-MIL-101(Cr) (770.08 cm^3/g STP), suggesting amine groups improve pore accessibility. However, NH_2-MIL-101(Cr)'s hysteresis loop shows a more pronounced divergence (47-55 units), likely due to differences in pore geometry or metal center interactions (Cr vs. Cu) [43]. The H2-type hysteresis in NH_2-MIL-101(Cr) aligns with Xuan-Dong et al. (2011)'s study on mesostructured MIL-53(Al), which showed trimodal pore distributions and hysteresis from disordered wormhole-like structures. The loop's closure near P/P_o = 0.9 in NH_2-MIL-101(Cr), due to multilayer adsorption, mirrors MIL-53(Al), highlighting mesoporous architecture's role in hysteresis. However, NH_2-MIL-101(Cr)'s higher adsorbed quantity (up to 770 cm^3/g STP) indicates a larger pore volume or surface

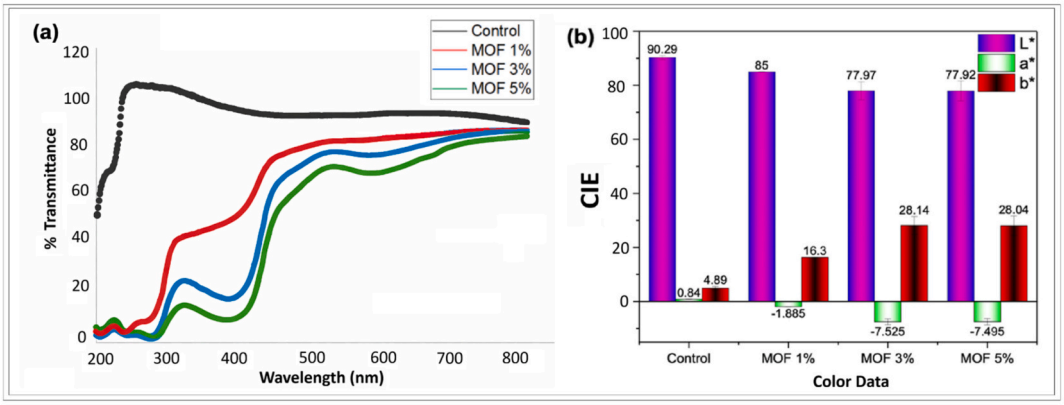

Fig. 6. (a) UV-Vis Transmittance Spectrum for Control, MOF 1%, MOF 3%, and MOF 5% treatments. (b) Color indices of NH_2-MIL-101(Cr) film at 1%, 3%, and 5% concentrations.

area, likely due to its chromium-based framework's stability and functionalization [44].

3.6. SEM analysis of the NH_2-MIL-101(Cr) film

The scanning electron microscopy (SEM) analysis was conducted to investigate the morphology and particle distribution of the control and NH_2-MIL-101(Cr) film at concentrations of 1%, 3%, and 5% (Fig. 5a–d). For the control and 1% film sample, the image revealed a relatively smooth surface with sparse, scattered particles and a central region exhibiting a defined structure, suggesting low particle density. The 3% film sample showed an increased presence of particles, appearing as small, dispersed clusters across the surface, indicating a moderate particle distribution. The 5% film sample exhibited the highest particle density, with more compact and numerous clusters, reflecting a significant increase in MOF content. The SEM results highlight a clear concentration-dependent trend in the morphology of the NH_2-MIL-101 (Cr) film. The sparse particle distribution in the 1% film suggests a low loading of MOF, resulting in minimal surface coverage. As the concentration increased to 3%, the formation of small clusters indicates improved particle aggregation, likely due to enhanced intermolecular interactions or nucleation sites at higher MOF content. The 5% film, with its dense and compact clusters, demonstrates a saturation effect, where increased MOF concentration leads to greater particle packing and potential agglomeration. The presence of a uniform, layered structure across all samples confirms the film matrix, aligning with the preparation method where the MOF was deposited as a thin film.

The SEM findings in this study were compared with relevant literature focusing on MOF films. Pak et al. (2022) reported SEM analysis of MOF-5-based composite films with hydrocolloids, observing increased particle density with higher MOF loading, like the trend in our 3% and 5% NH_2-MIL-101(Cr) films, suggesting potential antibacterial applications [6]. Su and Lee (2018) characterized KOH/M050 composite films, noting enhanced flexibility and particle distribution with functionalization, which aligns with the improved clustering in our 5% film, indicating suitability for humidity sensing [45]. Park et al. (2017) described SEM of thin-film composite (TFC) reverse osmosis membranes with MOF-modified polysulfone layers, showing a smooth, thin active layer with increased porosity, paralleling the layered structure and density increase in our films, which could enhance desalination performance [24].

Tokalıoğlu et al. (2017) reported SEM analysis of MOF-545 powders with high porosity and irregular shapes, resembling the micrometer-sized clusters in our MOF samples, supporting their use in heavy metal adsorption [46]. Marak et al. (2025) used SEM to confirm the integrity of β-CD-MOF powders post-piperine encapsulation, noting slight size increases (429.63 nm to 463.80 nm), which parallels the increased particle density in our MOF 5% sample, indicating stability enhancements [47]. Hassanpour et al. (2015) described SEM of magnetic MOF nanocomposites showing aggregated particles, consistent with our MOF 3% and 5% clusters, enhancing heavy metal sorption capacity [48]. Overall, the irregular clustering and concentration-dependent morphology in our study align with prior SEM observations of MOF powders, though the less uniform particle sizes compared to highly optimized MOFs suggest synthesis-specific variations that could be refined for enhanced performance.

3.7. UV-Vis spectra and transmittance analysis of samples

Ultraviolet-Visible (UV-Vis) spectroscopy is an important analytical technique for assessing the optical properties of materials, particularly MOF-polymer composites, as it provides insights into absorbance, transmittance, and electronic transitions across a wide wavelength range (200–800 nm). This method enables the evaluation of UV shielding capability and optical transparency, both of which are critical for applications such as packaging, protective coatings, and electronic devices.

The UV-Vis transmittance spectra in Fig. 6a reveals distinct trends across the treatments. The control sample exhibits the highest transmittance, starting at approximately 89.3% at 800 nm and decreasing gradually to 83.3% at 700 nm, with no significant UV shielding due to the absence of MOFs. The MOF 1% treatment shows a slight reduction, with transmittance dropping from 85.0% at 800 nm to 83.5% at 700 nm, indicating minimal UV absorption and retaining high transparency. The MOF 3% treatment demonstrates a more pronounced decrease, with transmittance ranging from 86.1% at 800 nm to 85.1% at 700 nm, suggesting enhanced UV shielding, particularly in the 300–400 nm range (UVA), where a subtle decline is observed. The MOF 5% treatment further reduces transmittance, starting at 86.1% at 800 nm and falling to 85.0% at 700 nm, with a more noticeable absorption in the UV region (below 400 nm), indicating improved shielding efficiency with higher MOF content. All samples maintain relatively high visible light transmittance (above 83%) at 600 nm, though it decreases slightly with increasing MOF concentration, reflecting a trade-off between UV shielding and optical clarity.

The analysis indicates that the incorporation of NH_2-MIL-101(Cr) enhances UV shielding, with the effect becoming more significant at 3% and 5% MOF loadings. The gradual reduction in transmittance with increasing MOF content aligns with the increased absorption due to metal-ligand charge transfer or electronic transitions within the chromium-based framework. However, the limited data below 700 nm (not fully provided) indicates that the full UV range (200–400 nm) may show more substantial shielding, particularly for UVB (280–320 nm) and UVC (200–280 nm), which requires further investigation. The

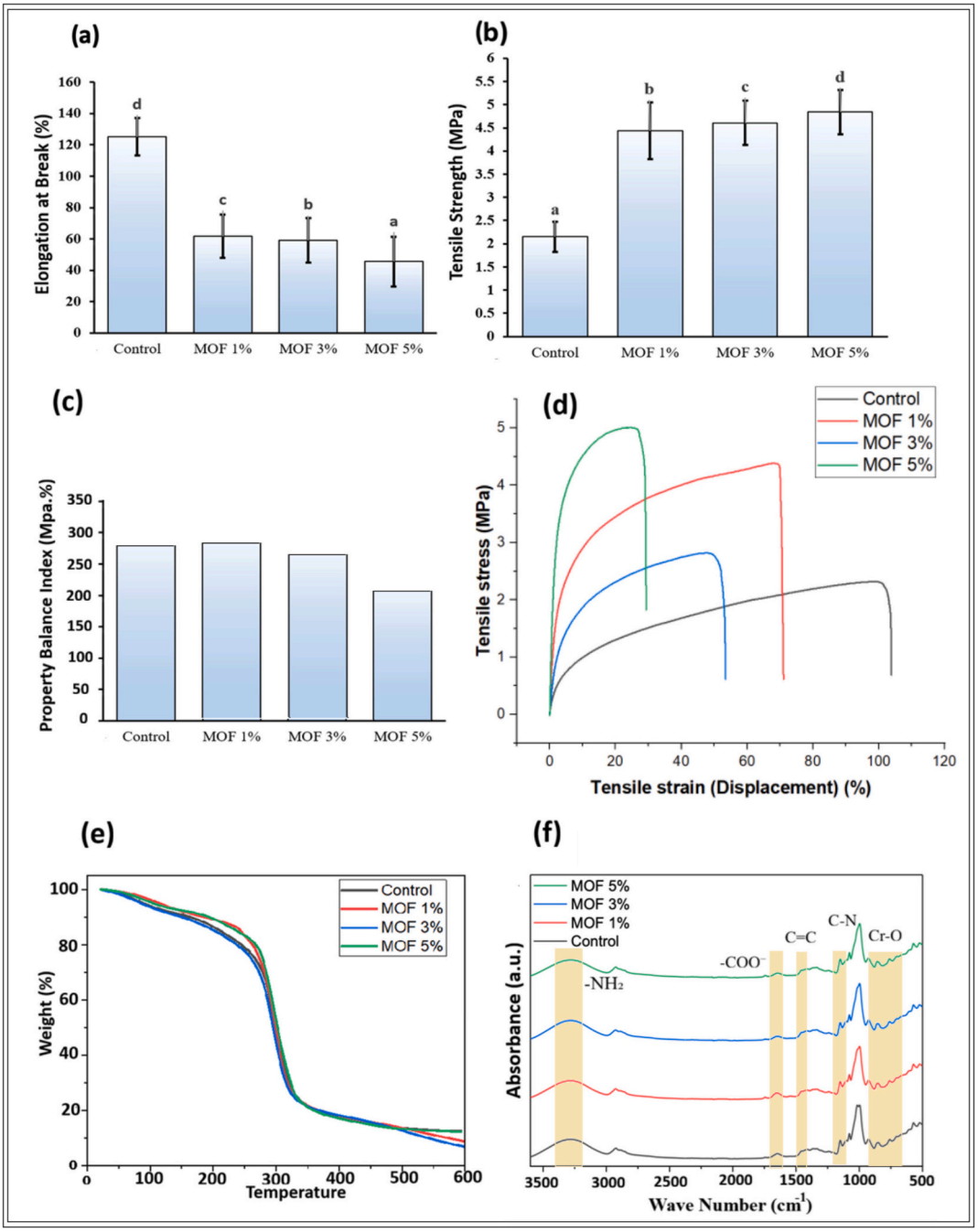

Fig. 7. (a) Elongation at Break (%) of NH_2-MIL-101(Cr) films across all treatments. (b) Tensile Strength (MPa) of NH_2-MIL-101(Cr) films across all treatments. (c) Property balance index (PBI), defined as the product of tensile strength and elongation at break, illustrating the trade-off between strength and toughness of the composite films at different MOF loadings. (d) Stress-Strain curves of NH_2-MIL-101(Cr) films across all treatments. (e) TGA Curves of NH_2-MIL-101(Cr) films across all treatments. (f). FTIR Spectra of NH_2-MIL-101(Cr) Film at 1%, 3%, and 5% Concentrations.

control's lack of UV absorption contrasts with the MOF-treated samples, highlighting the role of MOFs in optical modification.

Sun et al. (2021) reported MIL-125(Ti)-NH_2@cellulose bioplastics with robust UV-blue shielding, blocking nearly all UVB below 320 nm (75.5% transmittance at 600 nm) and 100% UV with 66% transmittance, maintaining photostability over 12 h, indicating that the films in this study, with transmittance above 83% at 600 nm with 5% MOF, offer superior visible clarity but potentially less effective UVB/UVC shielding [49]. Sun et al. (2023) demonstrated complete UV shielding and photostability in Cu-MOF/cellulose films, aligning with the absorption trend observed in this study, though the chromium-based NH_2-MIL-101(Cr) structure may exhibit different absorption peaks [50]. Chen et al. (2021) showed CA/Cu-MOF nanocomposite films with superior UV shielding across the entire UV range and 12-h photostability, retaining high visible transparency, suggesting that the films in this study may lag in UV blocking efficiency despite similar transparency trends [29]. Hong et al. (2024) reported Gel/Carr/ZC films with 97.82% UV-blocking and high transparency, surpassing the UV shielding in this study, likely due to the enhanced stability of ZC-MOF [51].

The NH_2-MIL-101(Cr) films in this study exhibit a dose-dependent increase in UV shielding with high visible transmittance (>83% at 600 nm), suitable for transparent UV-protective applications. They align with cellulose-MOF trends in shielding behavior but show reduced UVB/UVC blocking compared to MIL-125(Ti)-NH_2, Cu-MOF, and ZC-MOF

systems, pending full wavelength data.

3.8. Color analysis of the NH_2-MIL-101(Cr) film

The color analysis of the NH_2-MIL-101(Cr) film was conducted to evaluate the optical properties and structural changes across different MOF concentrations (1%, 3%, and 5%), as depicted in Fig. 6b. This analysis utilizes CIE Lab* color space parameters (L for lightness, a for green-red axis, and b for blue-yellow axis) to quantify the color evolution, providing insights into MOF loading, particle aggregation, and potential applications.

The 1% film exhibits the highest lightness (L = 84.95), close to the standard (L = 89.80), with a slightly negative a (-1.89) indicating a faint green tint and a positive b (16.33) suggesting a yellowish hue. This reflects a low MOF loading, resulting in minimal light absorption and a near-transparent appearance, consistent with sparse particle distribution observed in SEM. The chroma (C = 16.44) and hue angle (h = 96.61°) indicate a moderately saturated yellow-green color. The high reflectance (%R = 31.82) and low absorption coefficient (K/S = 0.7304) support the light color and thin film layer.

The 3% film shows a significant decrease in lightness (L = 75.60), with a more negative a (-8.26) and a higher b (30.48), indicating a stronger green shift combined with a pronounced yellow component. This results in a darker, more saturated color (C = 31.58, h = 105.16°), suggesting increased MOF content and particle clustering, which enhances light scattering and absorption. The low reflectance (%R = 7.39) and high absorption coefficient (K/S = 5.8044) confirm greater optical density, aligning with the moderate particle aggregation seen in SEM.

The 5% film has an intermediate lightness (L = 80.53), with a negative a (-6.69) and a high b (25.48), indicating a green-yellow hue that is darker than the 1% film but less saturated than the 3% film (C = 26.34, h = 104.71°). This suggests a saturation effect, where increased MOF loading leads to dense clustering and potential agglomeration, as observed in SEM. The reflectance (%R = 12.19) is higher than 3% but lower than 1%, and the absorption coefficient (K/S = 3.1641) is lower than 3% but higher than 1%, indicating a balanced optical response due to compact particle packing.

The color shift from 1% to 3% and 5% is driven by the electronic structure of Cr^{3+} centers and amine-functionalized ligands in NH_2-MIL-101(Cr). The increase in negative and positive b with concentration reflects enhanced d-d transitions or ligand-to-metal charge transfer (LMCT), likely due to denser MOF networks. The uniform layered structure from SEM supports the consistent color distribution across samples.

The color analysis reveals a clear trend: lightness decreases from 1% to 3% due to an increase in MOF loading, then slightly recovers at 5% possibly due to scattering from dense clusters. The value becomes more negative (greener) and b increases (yellower) from 1% to 3%, with a slight moderation at 5%, indicating a peak saturation at 3% followed by agglomeration effects. The reflectance decreases and K/S increases with concentration, peaking at 3%, reflecting the highest optical density at this level.

The color results are compared with MOF-based films reporting L*a*b* or visual color changes. Riahi et al. (2023) reported gelatin/PVA films with Cu-MOFs, showing L values decreasing from ~85 to ~70 and a shift from positive to negative a with pH/ammonia exposure, similar to our 1% to 3% transition, suggesting a comparable MOF loading effect for intelligent packaging [52]. Zhang et al. (2024) noted Co-MOF/CMC-Na films with ΔE correlated to freshness, showing a decrease in L and increase in b, aligning with our 3% and 5% darkening, supporting freshness monitoring potential [53]. Teymouri et al. (2025) observed Cu-MOF@agar films with L decreasing and a/b varying widely (blue to brown), paralleling our green-yellow shift, enhancing real-time fish monitoring [54]. Tao et al. (2024) reported CA/Co-MOF films with L reduction and color changes to green/brown, consistent with our 5% hue, indicating pork preservation suitability [55].

The color analysis indicates that the 1% film's high lightness suits transparent applications like optical coatings, while the darker 3% and 5% films, with enhanced green-yellow hues, are promising for light-absorbing applications like sensors or catalytic films. The concentration-dependent trends highlight tunable optical properties, with 3% offering maximum color intensity and 5% showing saturation effects, which could be tailored for specific uses.

3.9. Mechanical tensile analysis of NH_2-MIL-101(Cr) films

Tensile testing is a crucial method for evaluating the mechanical strength and flexibility of MOF-polymer composites, providing essential insights into their durability and suitability for structural applications under mechanical stress. This analysis helps assess the impact of MOF incorporation on mechanical performance, guiding the development of materials for practical use. The tensile properties of NH_2-MIL-101(Cr) films across control, MOF 1%, MOF 3%, and MOF 5% treatments are assessed, with data presented in elongation at break (Fig. 7a), and tensile strength (Fig. 7b).

The tensile stress results indicate a significant enhancement with MOF incorporation. The control sample exhibits an average tensile stress of 2.15 MPa, while MOF 1%, MOF 3%, and MOF 5% treatments show increases to 4.44 MPa, 4.61 MPa, and 4.84 MPa, respectively, with standard deviations of 0.61, 0.48, and 0.48 MPa. This suggests a dose-dependent improvement in stress resistance, likely due to the reinforcing effect of the chromium-based MOF framework within the polymer matrix. The tensile strength data in Fig. 7b further supports this trend, with maximum stress values rising from 4.38 MPa (MOF 1%) to 4.74 MPa (MOF 5%), reflecting enhanced load-bearing capacity with increasing MOF content. However, the elongation at break, shown in Fig. 7a, decreases from 125.16% (control) to 61.77%, 59.14%, and 45.59% for MOF 1%, MOF 3%, and MOF 5%, respectively, with standard deviations of 11.90%, 14.23%, and 15.86%, indicating reduced flexibility as MOF concentration increases, possibly due to increased rigidity or agglomeration. To quantitatively assess the trade-off between tensile strength and toughness, a property balance index (PBI), defined as the product of tensile strength and elongation at break, was calculated. As shown in Fig. 7c while MOF 5% exhibited the highest tensile strength, its PBI decreased markedly due to severe loss of elongation. In contrast, the MOF 3% composite retained a high PBI while achieving substantial strength enhancement, confirming 3% as the optimal MOF loading for balanced mechanical performance. In addition, as observed in Fig. 7d with increasing MOF loading, the tensile strength of the films improves; however, the elongation at break decreases, indicating a reduction in flexibility.

Chen et al. (2021) reported CA/Cu-MOF films with improved tensile strength due to good MOF compatibility, outperforming the control but with similar flexibility reduction, supporting the observed trend [29]. Elangovan et al. (2011) reported a 15% increase in Izod impact strength and 170% in elongation for PLLA-MOF composites (1–5 wt%), reducing brittleness, contrasting with the NH_2-MIL-101(Cr) films' decline in strength (from 9.95 to 2.15 MPa) and strain (from 260% to 125%), possibly due to agglomeration or differences in copper-based MOFs versus chromium-based NH_2-MIL-101(Cr) and matrix compatibility. Yang et al. (2021) noted a modulus increase in PCN-222/PMMA composites up to 0.5 wt% per the Halpin-Tsai model, differing from the NH_2-MIL-101(Cr) decline, likely due to uncontrolled aspect ratio or aggregation [56]. Qian et al. (2018) observed strength gains (17.20 MPa dry) in cellulose-ZIF-67 with CNF reinforcement, contrasting the NH_2-MIL-101(Cr) trend, suggesting the role of additional reinforcement [57]. Peterson et al. (2021) highlighted MOF-polymer synergies (e.g., 500% damping increase), indicating NH_2-MIL-101(Cr)'s decline may result from poor matrix integration [58].

In this study, the NH_2-MIL-101(Cr) films in this study demonstrate a significant improvement in tensile stress and strength with increasing MOF content, suitable for applications requiring enhanced mechanical

resistance. However, the decrease in elongation at break suggests a need for optimization to balance strength and flexibility, potentially through improved MOF dispersion or matrix compatibility, warranting further investigation.

3.10. Thermogravimetric analysis (TGA)

Thermogravimetric analysis (TGA) is a vital technique for evaluating the thermal stability and decomposition behavior of polymer-metal-organic framework (MOF) composites, providing essential insights into their suitability for high-temperature applications such as packaging or structural materials. The primary purpose of this analysis is to assess how varying MOF concentrations and material compositions influence the thermal degradation profiles of NH_2-MIL-101(Cr) films, guiding the optimization of their thermal performance.

The TGA curve in Fig. 6e illustrates the thermal decomposition behavior of NH_2-MIL-101(Cr) films across all treatments, revealing distinct weight loss profiles, with all samples exhibiting an initial minor weight loss (2-5%) below 100 °C, attributed to the evaporation of adsorbed water or residual solvents, a common feature of MOF-polymer composites due to their porosity. The control treatment shows thermal decomposition beginning at approximately 230 °C, with a weight loss of about 60% by 400 °C and a residue of 10% at 600 °C, indicating lower thermal stability without MOF reinforcement. For the MOF 1% treatment, the primary decomposition starts around 250 °C, with a weight loss of approximately 40% by 400 °C, likely due to the degradation of the polymer matrix and partial breakdown of the MOF framework (which remains stable up to 300–350 °C), resulting in a residue of about 20% at 600 °C, reflecting moderate thermal stability with low MOF content. The MOF 3% treatment shifts the decomposition onset to 270 °C, with a 45% weight loss by 400 °C, possibly due to enhanced MOF-polymer interactions, and a residue of 25% at 600 °C, indicating increased char formation likely due to better MOF distribution. For the MOF 5% treatment, the decomposition onset moves to 290 °C, with a 50% weight loss by 400 °C, suggesting improved initial stability from higher MOF density, though the residue drops to 18% at 600 °C, potentially due to excessive MOF agglomeration. The overall trend indicates that thermal stability (decomposition onset temperature) increases with MOF concentration up to 3% but may slightly decline at 5% due to agglomeration effects overpowering the stabilizing influence of MOFs.

Compared to prior studies, Elangovan et al. (2011) reported no significant thermal stability improvement in PLLA-MOF composites (1–5 wt%), contrasting with the enhanced onset temperatures in NH_2-MIL-101(Cr) films, possibly due to differences in MOF type (copper-based vs. chromium-based) and matrix interactions [59]. Yang et al. (2021) noted improved stability in PCN-222/PMMA composites due to restricted polymer chain mobility, aligning with the higher residue in MOF 3%, suggesting optimal dispersion enhances thermal performance[55]. Gandara-Loe et al. (2020) observed stable UiO-67@PU nanocomposites with prolonged drug release, differing from the residue decline in NH_2-MIL-101(Cr) at 5%, likely due to better MOF integration in PU [60]. Khan et al. (2021) found thermal stability in ZIF-67/PVA-starch composites increased up to 4 wt% but declined at 10 wt% due to aggregation, mirroring the NH_2-MIL-101(Cr) trend at 5%, indicating an optimal loading threshold [9]. Ananthi et al. (2023) reported enhanced stability with Fe-MIL-88A in cellulose acetate, contrasting with NH_2-MIL-101 (Cr)'s decline at higher loadings, possibly due to additional reinforcing agents [7]. Wang et al. (2019) and Zhang et al. (2025) focused on electrochemical and triboelectric applications with limited TGA data, but their emphasis on MOF-polymer synergy suggests NH_2-MIL-101 (Cr)'s decline may stem from poor matrix integration [61,62]. The analysis suggests that the 1% film (MOF 1%) provides moderate thermal stability, suitable for low-temperature applications, while the 3% film (MOF 3%) offers an optimal balance with enhanced stability and higher char yield, ideal for moderate-temperature uses. The 5% film (MOF 5%) exhibits initial stability but a reduced residue due to agglomeration, limiting its effectiveness at high temperatures. The shift in decomposition onset and residue trends points to an optimal MOF loading around 3%, beyond which agglomeration negates thermal benefits. While the present study focuses on NH_2-MIL-101(Cu) synthesized via an aqueous, environmentally friendly route, a direct experimental comparison with films incorporating DMF-synthesized NH_2-MIL-101(Cr) could further clarify the isolated effects of synthesis solvent on MOF–polymer composite performance. However, such a comparison would introduce additional variables related to the different metal centers (Cu vs. Cr), which are known to intrinsically influence crystallinity, surface area, and thermal–mechanical behavior. A systematic study using identical metal nodes with parallel green and DMF-based synthesis routes is therefore identified as an important direction for future work.

3.11. FTIR of the NH_2-MIL-101(Cr) film

Fourier Transform Infrared (FTIR) spectroscopy analysis was performed toward elucidating the chemical composition, functional groups, and structural changes in the NH_2-MIL-101(Cr) film across different concentrations (1%, 3%, and 5%), as depicted in Fig. 6f. This technique provides important insights into the molecular interactions and stability of the film, which are influenced by the MOF loading and preparation conditions.

The FTIR spectra of the NH_2-MIL-101(Cr) film exhibit characteristic absorption bands associated with the metal-organic framework's organic ligands and metal coordination. A broad band in the range of 3400–3200 cm^{-1} is observed, attributable to the stretching vibrations of the -NH_2 groups attached to the benzene rings of the 2-aminoterephthalate ligand, with varying intensity across concentrations. For the 1% film, this band appears weaker, suggesting a lower density of amine groups due to minimal MOF loading. As the concentration increases to 3% and 5%, the intensity of this band enhances, reflecting a higher incorporation of NH_2-MIL-101(Cr) and increased intermolecular hydrogen bonding between amine groups, which is indicative of improved film uniformity. A sharp peak around 1650–1600 cm^{-1}, corresponding to the asymmetric stretching of the carboxylate groups ($sCOO^-$) coordinated to the Cr^{3+} centers, is prominent in all samples. This peak's position remains consistent across the 1%, 3%, and 5% films, confirming the stability of the Cr-O coordination bonds within the MOF framework, regardless of concentration. However, a slight shift or broadening at 3% and 5% may suggest enhanced interactions between carboxylate groups and the film matrix, possibly due to an increase in MOF packing.

The aromatic C═C stretching vibrations of the benzene ring appear in the range of 1500–1450 cm^{-1}, with a noticeable increase in intensity from 1% to 5%, reflecting the growing proportion of the organic linker in the film. This trend supports the SEM observations of increased particle density with higher MOF content. Additionally, a band around 1250–1200 cm^{-1}, associated with the C—N stretching of the amine group, becomes more defined at 3% and 5%, indicating a concentration-dependent enhancement of amine-related functionalities, which may contribute to the film's chemical reactivity. In the lower wavenumber region (below 1000 cm^{-1}), bands related to Cr—O stretching and bending modes are observed, typically around 600–800 cm^{-1}. These peaks remain stable across all concentrations, reinforcing the structural integrity of the Cr-based secondary building units (SBUs) in the film. However, a slight intensity increases at 5% could indicate a denser

Table 2
The performance of the present NH_2-MIL-101(Cr)/sago starch films in comparison with recent MOF-based packaging systems.

Matrix Polymer	MOF Type	MOF Synthesis Approach	Tensile Strength (MPa)	Elongation at Break (%)	TGA residue at 600 °C (%)	Decomposition onset (°C)	Visible transmittance 600 nm (%)	UV-blocking (%)	Reference
Sago starch	NH_2-MIL-101 (Cr)	Green aqueous (water-only) synthesis [1]	2.15 (0 % MOF), 4.61 (3 % MOF), 4.84 (5 % MOF)	125.2 (0 % MOF), 45.6 (5 % MOF)	10 (0 % MOF), 25 (3 % MOF), 18% at 5 % MOF)	230 (0 % MOF), 270 (3 % MOF), 290 (5 % MOF)	>83 %	Not Reported	Current Study
Potato starch	Cu/Na-MOF (novel Cu–Na framework)	Not specified – constructed Cu/Na-MOF filler)	11.6 % increase compared to control	Not Reported	Not Reported	Not Reported	Not Reported	96.1 % (UV shielding after 6 wt% MOF)	[69]
Carboxymethyl starch (CMS)/ PVA blend	Cu–L-tryptophan-derived MOF	Simple aqueous solution synthesis	42.92	Not Reported	Not Reported	Not Reported	2.4 %	≈97.6 % (implied from 2.4% transmittance)	[70]
Corn starch	Nano Fe-HIA complex	(Not specified – Fe-HIA formed in situ)	6.8	Not Reported	Not Reported	Not Reported	Not Reported	100 %	[71]

arrangement of Cr—O clusters, consistent with the saturation effect noted in SEM analysis.

The FTIR spectra reveals a clear concentration-dependent evolution in the film's chemical structure. The 1% of the film shows weaker absorption bands, suggesting a thin and less dense MOF layer with limited functional group exposure. At 3%, the intensified -NH_2 and -COO^- bands indicate a more robust MOF network, likely due to improved nucleation and film growth. The 5% film exhibits the strongest peaks, particularly for amine and aromatic vibrations, reflecting a saturated MOF layer with potential agglomeration, as corroborated by SEM data.

To better highlight the performance of the present NH_2-MIL-101(Cr)/ sago starch films in comparison with recent MOF-based packaging systems, a benchmarking comparison with representative studies reported in the literature is summarized in Table 2. The comparison includes mechanical, thermal, optical properties, as well as matrix type and MOF synthesis approaches. As shown in Table 2, although some reported MOF-based films exhibit higher tensile strength and stronger UV-blocking, the present system demonstrates competitive mechanical reinforcement and improved thermal stability while uniquely employing a fully green, aqueous MOF synthesis and a regionally abundant starch matrix, highlighting its sustainability advantage.

The FTIR findings align with studies on MOF-based films. Park et al. (2017) reported FTIR analysis of thin-film composite (TFC) reverse osmosis membranes with MOF-modified polysulfone layers, observing stable carboxylate and metal-oxygen bands, like the consistent Cr-O peaks in our NH_2-MIL-101(Cr) film, suggesting robust framework stability across multiple concentrations [24]. Su and Lee (2018) characterized KOH/M050 composite films, noting enhanced amine-related peaks with functionalization, which parallels the intensified -NH_2 bands in our 3% and 5% films, indicating improved chemical interactions. These comparisons suggest that the NH_2-MIL-101(Cr) film's concentration-dependent FTIR features could enhance its performance in applications like desalination or sensing [45]. The FTIR analysis confirms the presence of key functional groups (—NH_2, —COO^-, C═C) and the stability of the Cr-based framework in the NH_2-MIL-101(Cr) film. The concentration-dependent intensification of amine and aromatic bands highlights the film's tunable chemical properties, which could be leveraged for applications requiring specific surface functionalities, such as gas adsorption or catalytic processes. The stability of Cr—O vibrations across all concentrations underscores the film's structural resilience, making it a promising candidate for advanced material applications.

4. Conclusions

This study successfully developed a green, aqueous synthesis method for NH_2-MIL-101(Cr), eliminating the use of toxic organic solvents while preserving its high crystallinity, porosity (>1000 m^2/g surface area), and functional amino groups.

When this green-synthesized MOF was incorporated into sago starch films, the composite materials showed markedly improved properties. In particular, a 3 wt% MOF loading provided the best overall balance of performance: tensile strength roughly doubled (from 2.15 MPa for the neat starch film to about 4.6 MPa) and thermal stability increased substantially (onset of decomposition rising from ~230 °C to ~270 °C). A higher loading (5 wt%) produced the highest ultimate strength (4.84 MPa) but caused significant agglomeration and a sharp drop in film extensibility (elongation at break fell to ~46% from 125% in the control). This confirms that the 3 wt% formulation is optimal among the tested compositions. The MOF-containing films also demonstrated enhanced UV-blocking while maintaining good visible-light transparency, benefiting potential packaging applications.

Future work will focus on verifying the environmental and practical performance of these biocomposites. Key next steps include systematic biodegradability testing (for example, compost) to ensure that the NH_2-MIL-101(Cr)–starch films break down under realistic conditions, and long-term stability assessments (such as increased aging under heat or UV exposure) to evaluate shelf-life durability. In addition, comprehensive safety assessments, including metal-ion leaching studies and in vitro cytotoxicity evaluations, should be conducted to confirm the suitability of these materials for food-packaging and environmentally sensitive applications. Such studies will be crucial to establish the real-world sustainability and viability of the developed MOF-reinforced bioplastic packaging.

CRediT authorship contribution statement

Shima Jafarzadeh: Writing – review & editing, Writing – original draft, Validation, Supervision, Project administration. **Yasaman Esmaeili:** Methodology, Validation, Visualization, Writing – review & editing. **Moon Paul:** Methodology, Investigation. **Seyedeh Zahra Haeri:** Writing – original draft, Methodology, Investigation. **Colin J.**

Barrow: Writing – review & editing, Visualization, Validation, Supervision. **Mina Dokouhaki:** Writing – review & editing, Visualization. **Masoumeh Zargar:** Writing – review & editing, Visualization, Validation, Supervision. **Minoo Naebe:** Writing – review & editing, Visualization, Validation, Supervision.

Declaration of competing interest

The authors declare that they have no known competing financial interests or personal relationships that could have appeared to influence the work reported in this paper.

Data availability

Data will be made available on request.

References

[1] S. Jafarzadeh, M. Nooshkam, M. Zargar, F. Garavand, S. Ghosh, M. Hadidi, M. Forough, Green synthesis of nanomaterials for smart biopolymer packaging: challenges and outlooks, J. Nanostructure Chem. 14 (2024) 113–136.

[2] W. Yang, S. Liu, H. Ren, Y. Huang, S. Zheng, S. Li, Z. Ling, W. Fan, Y. Tian, L. Pan, Metal–organic frameworks (MOFs)-based materials in food packaging: A review, J. Mater. Sci. 59 (2024) 20157–20175.

[3] A. Sultana, A. Kathuria, K.K. Gaikwad, Metal–organic frameworks for active food packaging, A review, Environ. Chem. Lett. 20 (2022) 1479–1495.

[4] M.-L. Chen, S.-Y. Zhou, Z. Xu, L. Ding, Y.-H. Cheng, Metal-organic frameworks of MIL-100 (Fe, Cr) and MIL-101 (Cr) for aromatic amines adsorption from aqueous solutions, Molecules 24 (2019) 3718.

[5] P. Ananthi, K. Hemkumar, S. Subasini, A. Pius, Improved performance of metal-organic frameworks loaded cellulose acetate based film for packaging application, Int. J. Biol. Macromol. 237 (2023) 124041.

[6] Z. Riahi, S.J. Hong, J.-W. Rhim, G.H. Shin, J.T. Kim, High-performance multifunctional gelatin-based films engineered with metal-organic frameworks for active food packaging applications, Food Hydrocoll. 144 (2023) 108984.

[7] N.A. Khan, M.B.K. Niazi, F. Sher, Z. Jahan, T. Noor, O. Azhar, T. Rashid, N. Iqbal, Metal organic frameworks derived sustainable polyvinyl alcohol/starch nanocomposite films as robust materials for packaging applications, Polymers (Basel) 13 (2021) 2307.

[8] K. Huang, Y. Wang, Z. Xu, Z. Zou, Q. Tang, H. Li, D. Peng, Novel intelligent packaging films based on starch/PVA with Cu-ICA nanocrystal as functional compatibilizer for monitoring food freshness, Int. J. Biol. Macromol. 271 (2024) 132373.

[9] S. Jafarzadeh, M. Golgoli, M. Azizi-Lalabadi, J. Farahbakhsh, M. Forough, N. Rabiee, M. Zargar, Enhanced carbohydrate-based plastic performance by incorporating cerium-based metal-organic framework for food packaging application, Int. J. Biol. Macromol. 265 (2024) 130899.

[10] N. An, K. Li, Y. Wang, W. Shen, X. Huang, S. Xu, L. Wu, H. Huang, Biodegradable bio-film based on Cordyceps militaris and metal-organic frameworks for fruit preservation, Int. J. Biol. Macromol. 262 (2024) 130095.

[11] L. Jiang, F. Liu, F. Wang, H. Zhang, M. Kang, Development and characterization of zein-based active packaging films containing catechin loaded β-cyclodextrin metal-organic frameworks, Food Packag. Shelf Life 31 (2022) 100810.

[12] A. Khan, Z. Riahi, J.T. Kim, J.-W. Rhim, Gelatin/carrageenan-based smart packaging film integrated with Cu-metal organic framework for freshness monitoring and shelf-life extension of shrimp, Food Hydrocoll. 145 (2023) 109180.

[13] X. Zhao, T.-J. Shi, Y.-Y. Liu, L.-J. Chen, Porphyrinic metal–organic framework-loaded polycaprolactone composite films with a high photodynamic antibacterial activity for the preservation of fresh-cut apples, ACS Appl. Polym. Mater. 5 (2022) 560–566.

[14] Y. Zhang, S. Yuan, X. Chen, M. Chen, B. Sun, D. Kim, K. Yam, Potential of metal-organic frameworks to adsorb ethylene for fresh produce active packaging applications, Food Packag. Shelf Life 35 (2023) 101034.

[15] S.J. Hong, Z. Riahi, G.H. Shin, J.T. Kim, Poly (vinyl alcohol)-based multifunctional smart packaging films with carbon dots-loaded metal-organic frameworks for freshness indicator and shelf-life extension of shrimp, Prog. Org. Coat. 198 (2025) 108899.

[16] M.J. Kowsar, O.M. Jazani, G. Dini, M. Moghadam, Elevating thermal and mechanical performance: The role of MIL-101 (Cr) and NH2-MIL-101 (Cr) in epoxy adhesives, Colloids and Surfaces A: Physicochemical and Engineering Aspects 725 (2025) 137564.

[17] AK Singh, P Sharma, M Shrivastav, R Chaudhary, P Chauhan, A Banerjee, PRODUCTION OF BIODEGRADABLE PLASTIC FILM FROM POTATO AND SAGO STARCH, Journal of microbiology, biotechnology and food sciences 14 (4) (2025 Jan 27) e11143.

[18] M.M. Marvizadeh, N. Oladzadabbasabadi, A.M. Nafchi, M. Jokar, Preparation and characterization of bionanocomposite film based on tapioca starch/bovine gelatin/nanorod zinc oxide, Int. J. Biol. Macromol. 99 (2017) 1–7.

[19] T. Virtanen, G. Rudolph, A. Lopatina, B. Al-Rudainy, H. Schagerlöf, L. Puro, M. Kallioinen, F. Lipnizki, Analysis of membrane fouling by Brunauer-Emmett-Teller nitrogen adsorption/desorption technique, Sci. Rep. 10 (2020) 3427.

[20] Y. Li, J. Yang, L. Sun, B. Liu, H. Li, L. Peng, Crosslinked fish scale gelatin/alginate dialdehyde functional films incorporated with carbon dots derived from pomelo peel waste for active food packaging, Int. J. Biol. Macromol. 253 (2023) 127290.

[21] G. Rineksa, Y. Whulanza, M. Gozan, Mechanical characteristics of thermoplastic sago starch-based biopolymer composite reinforced with microcrystalline cellulose (MCC) as a potential surgical suture material, in: AIP Conf Proc, AIP Publishing LLC, 2025: p. 060002.

[22] N. Johnson, P. Thavarajah, A. Madurapperumage, N. Windsor, L. Tang, D. Thavarajah, Fourier-transform infrared spectroscopy: An inexpensive, rapid, and less-destructive tool for starch and resistant starch analysis from pulse flour, Plant Phenome J. 6 (2023) e20086.

[23] R. Abedi-Firoozjah, N. Ahmadi, S. Valaee, S. Zamanpour, M.H. Moradiyan, B. Bahramian, N. Oladzadabbasabadi, M. Tavassoli, E. Sadeghi, Unlocking the potential of cyclodextrin/metal–organic frameworks in food packaging systems: an exclusive review on the latest trends, Food Bioprocess Technol. 18 (2025) 5010–5037.

[24] Z. Teymouri, H. Shekarchizadeh, K. Karami, Innovative real-time monitoring of fish freshness via agar-based film embedded with Cu-MOF colorimetric indicators, Chem. Eng. J. 510 (2025) 161751.

[25] A.J.B. Campuzano, R.B. Rezende, N.C. Taborda, J.C. dos Santos, F.V. Pereira, T. H. Panzera, Physical and mechanical properties of fused deposition modelling PLA/carbon dot nanocomposites, Mater. Today Commun. 40 (2024) 110025.

[26] Y. Dixit, P. Yadav, H. Asnani, A.K. Sharma, Penicillium oxalicum for enzymatic degradation of starch/polyvinylpyrrolidone plastic film, Biomass Convers. Biorefinery (2025) 1–24.

[27] U. Yunus, M.E. Khan, S. Sadiq, M. Aamir, Z. Ullah, M.H. Bhatti, M. Sher, G.-S. Chaudhry, Methotrexate-loaded Fe-metal organic frameworks: Synthesis, characterizations, and drug release investigations, J. Drug Delivery Sci. Technol. 97 (2024) 105790.

[28] Y. Wu, Y. Luo, B. Zhou, L. Mei, Q. Wang, B. Zhang, Porous metal-organic framework (MOF) Carrier for incorporation of volatile antimicrobial essential oil, Food Control 98 (2019) 174–178.

[29] J. Yang, Y. Wang, M. Pan, X. Xie, K. Liu, L. Hong, S. Wang, Synthesis of magnetic metal-organic frame material and its application in food sample preparation, Foods 9 (2020) 1610.

[30] Y. Zhu, J. Ciston, B. Zheng, X. Miao, C. Czarnik, Y. Pan, R. Sougrat, Z. Lai, C.-E. Hsiung, K. Yao, Unravelling surface and interfacial structures of a metal–organic framework by transmission electron microscopy, Nat. Mater. 16 (2017) 532–536.

[31] S. Turner, O.I. Lebedev, F. Schröder, D. Esken, R.A. Fischer, G. Van Tendeloo, Direct imaging of loaded metal– organic framework materials (Metal@ MOF-5), Chem. Mater. 20 (2008) 5622–5627.

[32] J.P. Patterson, P. Abellan, M.S. Denny Jr., C. Park, N.D. Browning, S.M. Cohen, J. E. Evans, N.C. Gianneschi, Observing the growth of metal–organic frameworks by in situ liquid cell transmission electron microscopy, J. Am. Chem. Soc. 137 (2015) 7322–7328.

[33] J. Zhang, N. Cheng, B. Ge, Characterization of metal-organic frameworks by transmission electron microscopy, Adv. Phys. X 7 (2022) 2046157.

[34] M.S. Denny Jr., L.R. Parent, J.P. Patterson, S.K. Meena, H. Pham, P. Abellan, Q. M. Ramasse, F. Paesani, N.C. Gianneschi, S.M. Cohen, Transmission electron microscopy reveals deposition of metal oxide coatings onto metal–organic frameworks, J. Am. Chem. Soc. 140 (2018) 1348–1357.

[35] Tongxin Xiao, Kangyue Qiao, Guodong Hao, Songyao Du, Yue Wang, Sui Chao, Preparation and Photocatalytic Reduction Performance of Cr(VI) by NH_2-MIL-101 (Fe, Co) Composite Catalyst, Journal of Solid State Chemistry 335 (2025) 125580.

[36] N. Noorani, A. Mehrdad, A. Fatehi-Mollayousef, A. Niaei, The advancements in mixed matrix membranes containing MOFs and ionic liquids for CO2/N2 separation, Sci. Rep. 15 (2025) 26271.

[37] H.-Y. Zhang, C. Yang, Q. Geng, H.-L. Fan, B.-J. Wang, M.-M. Wu, Z. Tian, Adsorption of hydrogen sulfide by amine-functionalized metal organic framework (MOF-199): An experimental and simulation study, Appl. Surf. Sci. 497 (2019) 143815.

[38] X.-D. Do, V.-T. Hoang, S. Kaliaguine, MIL-53 (Al) mesostructured metal-organic frameworks, Microporous Mesoporous Mater. 141 (2011) 135–139.

[39] A.M. Pak, E.N. Zakharchenko, A.A. Korlyukov, V.V. Novikov, Antibacterial films of composite materials based on the biocompatible metal–organic framework MOF-5 and hydrocolloids, Russ. J. Coord. Chem. 48 (2022) 195–200.

[40] P.-G. Su, X.-H. Lee, Electrical and humidity-sensing properties of flexible metal-organic framework M050 (Mg) and KOH/M050 and AuNPs/M050 composites films, Sensors Actuators B Chem. 269 (2018) 110–117.

[41] H.M. Park, K.Y. Jee, Y.T. Lee, Preparation and characterization of a thin-film composite reverse osmosis membrane using a polysulfone membrane including metal-organic frameworks, J. Membr. Sci. 541 (2017) 510–518.
[42] Ş. Tokalıoğlu, E. Yavuz, S. Demir, Ş. Patat, Zirconium-based highly porous metal-organic framework (MOF-545) as an efficient adsorbent for vortex assisted-solid phase extraction of lead from cereal, beverage and water samples, Food Chem. 237 (2017) 707–715.
[43] T.R. Marak, C.M. Kumar, M.S. Kumar, N.L. Naik, H.M. Rashmi, B. Ashritha, Encapsulation of piperine in metal organic frameworks and evaluation of its stability, characteristics, in-vitro digestion and product fortification, Food and Bioproducts Processing 152 (2025) 64–73.
[44] A. Hassanpour, R. Hosseinzadeh-Khanmiri, M. Babazadeh, J. Abolhasani, E. Ghorbani-Kalhor, Determination of heavy metal ions in vegetable samples using a magnetic metal–organic framework nanocomposite sorbent, Food Addi. Contaminants: Part A 32 (2015) 725–736.
[45] Z. Zhang, Y. Zhang, C. Wang, X. Liu, H.R. El-Seedi, P.L. Gomez, S.M. Alzamora, X. Zou, Z. Guo, Enhanced composite Co-MOF-derived sodium carboxymethyl cellulose visual films for real-time and in situ monitoring fresh-cut apple freshness, Food Hydrocoll. 157 (2024) 110475.
[46] Q. Tao, Y. Xiao, X. Hu, H. Pang, F. Xiao, L. Li, M. Chen, H. Wang, Intelligent multi-colorimetric cellulose acetate/cobalt-based metal-organic framework antibacterial film and its application to pork preservation, Food Packag. Shelf Life 45 (2024) 101339.
[47] L. Sun, L. Li, X. An, X. Qian, Nano-metal organic framework for enhanced mechanical, flame retardant and ultraviolet-blue light shielding properties of transparent cellulose-based bioplastics, Polymers (Basel) 13 (2021) 2433.
[48] L. Sun, L. Li, Q. Fu, X. Qian, Green fabrication of transparent Copper (II)-imidazolate metal–organic framework/cellulose nanocomposite films for antibacterial and UV-shielding applications, Cellulose 30 (2023) 3569–3588.
[49] K. Chen, J. Yu, J. Huang, Q. Tang, H. Li, Z. Zou, Improved mechanical, water vapor barrier and UV-shielding properties of cellulose acetate films with flower-like metal-organic framework nanoparticles, Int. J. Biol. Macromol. 167 (2021) 1–9.
[50] S.J. Hong, A. Khan, Z. Riahi, G.H. Shin, J.T. Kim, A versatile smart packaging film functionalized with zinc/curcumin-based metal-organic frameworks for maintaining and monitoring peach (Prunus persica) freshness, Food Packag. Shelf Life 46 (2024) 101408.
[51] L. Qian, D. Lei, X. Duan, S. Zhang, W. Song, C. Hou, R. Tang, Design and preparation of metal-organic framework papers with enhanced mechanical properties and good antibacterial capacity, Carbohydr. Polym. 192 (2018) 44–51.
[52] G.W. Peterson, D.T. Lee, H.F. Barton, T.H. Epps III, G.N. Parsons, Fibre-based composites from the integration of metal–organic frameworks and polymers, Nat. Rev. Mater. 6 (2021) 605–621.
[53] D. Elangovan, I.E. Yuzay, S.E.M. Selke, R. Auras, Poly (L-lactic acid) metal organic framework composites: optical, thermal and mechanical properties, Polym. Int. 61 (2012) 30–37.
[54] J. Gandara-Loe, B.E. Souza, A. Missyul, G. Giraldo, J.-C. Tan, J. Silvestre-Albero, MOF-based polymeric nanocomposite films as potential materials for drug delivery devices in ocular therapeutics, ACS Appl. Mater. Interfaces 12 (2020) 30189–30197.
[55] Q. Zhang, C. Huang, Y. Tao, Y. Zhang, J. Cui, D. Wang, P. Wang, Y. Zhang, Flexible Triboelectric Nanogenerators Based on Cadmium Metal–Organic Framework/Eethyl Cellulose Composites as Energy Harvesters for Selective Photoinduced Bromination Reaction, Small 21 (2025) 2406623.
[56] P. Wang, X. Du, T. Chen, X. Hao, A. Abudula, K. Tang, G. Guan, A novel electroactive PPy/HKUST-1 composite film-coated electrode for the selective recovery of lithium ions with low concentrations in aqueous solutions, Electrochim. Acta 306 (2019) 35–44.
[57] L. Qian, D. Lei, X. Duan, S. Zhang, W. Song, C. Hou, R. Tang, Design and preparation of metal-organic framework papers with enhanced mechanical properties and good antibacterial capacity, Carbohydr Polym 192 (2018) 44–51.
[58] G.W. Peterson, D.T. Lee, H.F. Barton, T.H. Epps III, G.N. Parsons, Fibre-based composites from the integration of metal–organic frameworks and polymers, Nat Rev Mater 6 (2021) 605–621.
[59] D. Elangovan, I.E. Yuzay, S.E.M. Selke, R. Auras, Poly (L-lactic acid) metal organic framework composites: optical, thermal and mechanical properties, Polym Int 61 (2012) 30–37.
[60] J. Gandara-Loe, B.E. Souza, A. Missyul, G. Giraldo, J.-C. Tan, J. Silvestre-Albero, MOF-based polymeric nanocomposite films as potential materials for drug delivery devices in ocular therapeutics, ACS Appl Mater Interfaces 12 (2020) 30189–30197.
[61] Q. Zhang, C. Huang, Y. Tao, Y. Zhang, J. Cui, D. Wang, P. Wang, Y. Zhang, Flexible Triboelectric Nanogenerators Based on Cadmium Metal–Organic Framework/Eethyl Cellulose Composites as Energy Harvesters for Selective Photoinduced Bromination Reaction, Small 21 (2025) 2406623.
[62] P. Wang, X. Du, T. Chen, X. Hao, A. Abudula, K. Tang, G. Guan, A novel electroactive PPy/HKUST-1 composite film-coated electrode for the selective recovery of lithium ions with low concentrations in aqueous solutions, Electrochim Acta 306 (2019) 35–44.

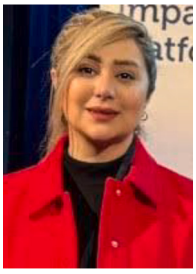

Shima Jafarzadeh Research Fellow at the Centre for Sustainable Bioproducts, School of Engineering, Deakin University, Australia. She is affiliated with the Faculty of Science, Engineering and Built Environment and is based at the Geelong Waurn Ponds Campus. Her research focuses on sustainable and bio-based materials, with particular interest in advanced biopolymers, functional nanomaterials, and their applications in food packaging and environmental sustainability. Dr Jafarzadeh is actively involved in interdisciplinary research aimed at developing high-performance, environmentally friendly materials.

Yasaman Esmaeili PhD student at School of Engineering, Deakin University, Australia. She is affiliated with the Faculty of Science, Engineering and Built Environment and is based at the Geelong Waurn Ponds Campus. Her research focuses on sustainable and bio-based materials, functional nanomaterials, and their applications in food packaging and environmental sustainability.

Moon Paul PhD student at Institute of Frontier Materials (IFM), Deakin University, Australia. She is working on smart and sustainable materials for real-world applications. Her current research focuses on thermomechanical recycling of polyolefin waste and the use of ionic liquids for polymer depolymerization. She has experience in multilayer plastic recycling, recycled plastic board manufacturing, sustainable graphene production from biomass, and development of graphene–polymer composites. With over ten years of laboratory experience, her expertise includes nanomaterial synthesis, materials characterisation, and plastic waste management.

Seyedeh Zahra Haeri She is a researcher with expertise in chemical engineering, advanced materials, polymers, and nanomaterials. Her research interests include nanomaterial synthesis, polymeric materials, nanostructured systems, and thin-film technologies. She has strong experience in material characterisation and nanoparticle synthesis, with a focus on developing and analysing functional polymer-based nanomaterials for advanced applications.

Colin J Barrow Chair of Biotechnology and Director of the Centre for Chemistry and Biotechnology at Deakin University, Australia. He holds a Ph.D. in marine natural products chemistry from the University of Canterbury, New Zealand, and an MBA from Penn State, USA. Formerly, he was Executive Vice President of Research and Development at Ocean Nutrition Canada. Professor Barrow's research spans natural products chemistry, biological chemistry, food biotechnology, and omega-3 oil technology, with a current focus on omega-3 biotechnology and amyloid fibres/nanomaterials. He has published ~130 peer-reviewed articles, holds multiple patents, and leads a research group including postdoctoral fellows and PhD students collaborating internationally.

Mina Dokouhaki Lecturer in Food Technology at RMIT University, where she actively contributes to teaching, research, and leadership within the Food Science and Nutrition discipline in the School of Science. Mina holds a BSc and MSc in Food Engineering from prestigious universities in Iran and a PhD in Chemical Engineering from the University of Melbourne. Her expertise primarily focuses on food biopolymers and colloids, bioactive compound delivery, surface chemistry, functional foods, emulsions, microencapsulation, and food processing.

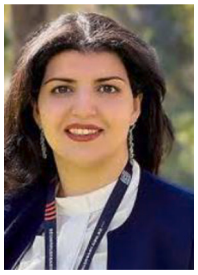

Masoumeh Zargar Senior Lecturer and ARC DECRA Fellow at the School of Engineering, Edith Cowan Uninersity (ECU), Australia and Co-Chair of the ECU Early and Mid-Career Researchers Network. She leads the Advanced Materials and Membranes Research Group, developing functional materials and membranes for water treatment, environmental remediation, energy transition, and food packaging. Dr Zargar holds a PhD in Chemical Engineering from the University of Adelaide and has received multiple awards and fellowships, including the ARC DECRA Fellowship and the ECU Engineering Staff Research Excellence Award, for her contributions to sustainable technologies and advanced materials.

Minoo Naebe Professor of Carbon Fibre and Composites and the founding Group Leader at Carbon Nexus within the Institute for Frontier Materials (IFM). The manufacture and use of carbon fibre and composite materials with potential to have significant impact on industry and manufacturing sectors is the major focus of Professor Naebe's research. The overarching aim is to use these materials to lightweight structures e.g in transportation where this leads to improved fuel efficiency and reduction in environmental emissions; and adding strength and functionalities. She has more than a decade's experience in carbon fibres and polymer composites and has successfully led several projects in collaboration with local and international industry partners in transport, energy and construction. Professor Naebe has led research into the development of carbon fibre from sustainable, low-cost precursors and her research has led into several commercial outcomes including a spin-off company at Deakin Manufacture.